

Robotic Arm Platform for Multi-View Image Acquisition and 3D Reconstruction in Minimally Invasive Surgery

Alexander Saikia¹, Chiara Di Vece¹, Sierra Bonilla¹, Chloe He¹, Morenike Magbagbeola¹,
Laurent Mennillo¹, Tobias Czempiel^{1,2}, Sophia Bano¹ and Danail Stoyanov¹

Abstract—Minimally invasive surgery (MIS) offers significant benefits such as reduced recovery time and minimised patient trauma, but poses challenges in visibility and access, making accurate 3D reconstruction a significant tool in surgical planning and navigation. This work introduces a robotic arm platform for efficient multi-view image acquisition and precise 3D reconstruction in MIS settings. We adapted a laparoscope to a robotic arm and captured ex-vivo images of several ovine organs across varying lighting conditions (operating room and laparoscopic) and trajectories (spherical and laparoscopic). We employed recently released learning-based feature matchers combined with COLMAP to produce our reconstructions. The reconstructions were evaluated against high-precision laser scans for quantitative evaluation. Our results show that whilst reconstructions suffer most under realistic MIS lighting and trajectory, many versions of our pipeline achieve close to sub-millimetre accuracy with an average of 1.05 mm Root Mean Squared Error and 0.82 mm Chamfer distance. Our best reconstruction results occur with operating room lighting and spherical trajectories. Our robotic platform provides a tool for controlled, repeatable multi-view data acquisition for 3D generation in MIS environments which we hope leads to new datasets for training learning-based models.

I. INTRODUCTION

Surgery has experienced remarkable evolution, particularly with the rise of minimally invasive techniques like endoscopy and laparoscopy. These methods have transformed modern surgical practice by reducing patient recovery time and minimizing tissue damage. However, they also present challenges, such as limited visibility, reduced tactile feedback, and increased cognitive demands on surgeons. As surgical techniques continue to advance, there is an increasing need for innovative technologies to address these challenges, enhance precision, and improve patient outcomes [1]. In minimally invasive surgery (MIS) and especially robot-assisted minimally invasive surgery (RAMIS), endoscopy is crucial for navigating the surgical field. Moreover, accurate and reliable 3-dimensional (3D) reconstruction of organs

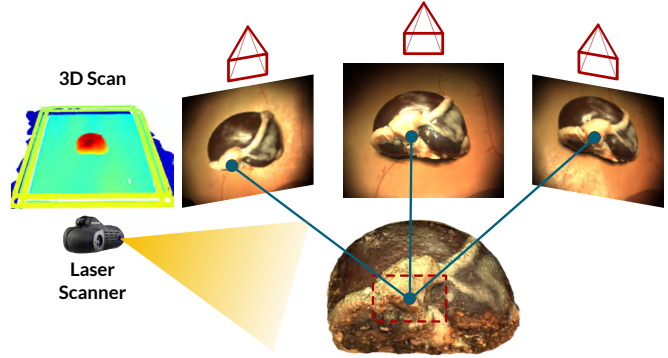


Fig. 1. This work creates 3D reconstructions from multi-view images collected by our robotic arm platform. We use a laser scanner to obtain ground truth data for comparison.

during surgery is vital for advancing downstream computer-assisted tasks, such as augmented and virtual reality [2], [3] and enhanced visualisation for surgical navigation [4]. Tools accomplishing these downstream tasks can augment the surgeon's understanding of the operating field and enable the identification of key structures such as blood vessels and tumours, improving both safety and precision in MIS and RAMIS [5]. However, the process of producing 3D reconstructions is challenging owing to the complexity of the surgical environment and the limited availability of image data with adequate 3D ground truth.

This work presents a robotic arm-based platform that addresses these challenges by enabling multi-view image acquisition and 3D reconstruction in MIS environments. By utilising a robotic arm we ensure more consistent, reliable scanning as well as obtaining pose information. The system is designed to accommodate various imaging modalities and employs a laser scanner to capture highly accurate 3D ground truth, allowing for comprehensive evaluation of the reconstruction pipeline as seen in Figure 1. Our approach utilises state-of-the-art feature matching methods, such as ALIKED [10] and GIM [11], paired with LightGlue (LG) [12] for robust correspondence across frames, and COLMAP [13], [14] for dense 3D reconstruction. The platform is validated by the collection and processing of multiple *ex-vivo* organ datasets, and its performance is benchmarked against ground truth laser scans to demonstrate the accuracy and robustness of the proposed system.

*This work was supported in whole, or in part, by the Wellcome/EPSRC Centre for Interventional and Surgical Sciences (WEISS) [203145/Z/16/Z], the Department of Science, Innovation and Technology (DSIT) and the Royal Academy of Engineering under the Chair in Emerging Technologies programme; EPSRC Centre for Doctoral Training in Intelligent, Integrated Imaging In Healthcare (i4health) [EP/S021930/1]. For the purpose of open access, the author has applied a CC BY public copyright licence to any author accepted manuscript version arising from this submission.

¹A. Saikia, C. Di Vece, S. Bonilla, C. He, L. Mennillo, T. Czempiel, S. Bano and D. Stoyanov are with the UCL Hawkes Institute, the Department of Medical Physics and Biomedical Engineering and the Department of Computer Science, University College London, London, United Kingdom

² T. Czempiel is with EnAcuity Ltd., London, United Kingdom.

Corresponding author: alexander.saikia.21@ucl.ac.uk

TABLE I

TABLE SUMMARY OF PUBLICLY AVAILABLE DATASETS IN SURGICAL DOMAIN WITH GROUND TRUTH PROPERTIES AND SIZE.

Dataset	System & Imaging Modality	Ground Truth Modality	Scenes	Size (frames)
CV3D [6]	Synthetic Colonoscopy	Synthetic	Simulated colonoscopy scenes	30073
SCARED [7]	Stereo (da Vinci Xi)	Structured Light Depth	Porcine Abdomen	17607
SERV-CT [8]	Stereo (da Vinci)	CT-based Segmentation	Porcine liver, kidney, heart	32
StereoMIS [9]	Stereo (da Vinci Xi)	Stereo Depth Estimation	Porcine and human	14804
Ours	Multi-view (Kinova Gen 3)	Laser Scans	Ovine liver, kidney	29806

Our main contributions and 3D reconstruction pipeline for surgery can be summarised as:

- We customise a robotic arm platform adding a laparoscopic system suitable for medical applications;
- We demonstrate our acquisition protocol with different design choices such as trajectories and lighting to account for high realism and adaptability to the medical domain;
- We show how the multi-view images taken by the system can be used to extract 3D reconstructions using established algorithm choices and comparing them with each other both qualitatively and quantitatively using relevant metrics.

Our platform represents a step towards semi-automatic 3D reconstruction of organs, which has the potential of being translated to surgical vision enhancement such as registration of pre-operative data such as MRI or PET, surgical measurements and advanced visualisation and guidance to aid the surgeon whereby improving patient outcome.

II. RELATED WORK

A. Datasets

The field of RAMIS has seen significant advancements, improving the safety, ease, and effectiveness of procedures [15], [16], [17]. The use of 3D visualisation in MIS to enhance surgical views has been shown to be beneficial for outcomes [18]. Therefore to reap this benefit, high quality data is essential for the development of algorithms for RAMIS [19]. However, despite the growing use of RAMIS, publicly available datasets with robot kinematics/poses and ground truth 3D information are rare due to logistical and ethical constraints. Current datasets often suffer from significant limitations in terms of size, realism and ground-truth accuracy, leading to concerns about their ability to generalise. Table I includes a list of commonly used datasets.

For example, CV3D [6] is a synthetic colonoscopy dataset comprising 22 short video sequences generated using phantom data. Given the synthetic nature of the dataset, the additional 3D data is accurate and reliable; however, the dataset lacks anatomical realism which poses challenges when training deep learning models.

The most commonly used dataset is SCARED [7], a stereo dataset obtained using a da Vinci Xi surgical robot. The ground truth was produced by obtaining 4 or 5 keyframes using structured light. Using the kinematics available from the robot, approximate depth maps were obtained by reprojecting depth maps from a keypoint. The SCARED dataset

has time synchronization issues between the Red-Green-Blue (RGB) video and kinematics, as well as ground truth depth misalignment with the RGB data. Some data has inaccurate intrinsic calibrations, which will affect point cloud reprojections and stereo rectification.

The SERV-CT [8] dataset is a validation dataset that offers 16 stereo-endoscopic image pairs acquired using the da Vinci surgical robot, each with computerised tomography (CT)-based anatomical segmentations and occlusion maps. The comparatively small sample size, limited to 16 pairs, increases the risk of overfitting if used as the primary training dataset.

StereoMIS [9] is an in-vivo dataset recorded using a da Vinci Xi surgical robot consisting of 3 porcine and 3 human subjects. Similar to SCARED, the ground truth poses are derived from the da Vinci's forward kinematics. While no ground truth depth data is available, the stereo images can be processed, and the single camera stream can be used to investigate monocular techniques. In creating a new platform for dataset acquisition we aim to address the significant complexity in creating a new surgical 3D dataset.

B. 3D Reconstruction for Surgery

After the collection of multi frame surgical data, 3D reconstruction is essential to enhance the surgeon's view and proceed with downstream tasks. There are numerous 3D reconstruction algorithms, including Structure from Motion (SfM), Simultaneous Localisation and Mapping (SLAM) and, if a stereo endoscope is used, stereo reconstruction [20], [21]. These algorithms rely on feature extraction and matching between 2-dimensional (2D) images for generating 3D point clouds, which are used to estimate depth and camera pose. Traditional feature extraction and matching methods like SIFT [22] have been widely used for this purpose. However, in surgical environments, particularly when dealing with low-texture organs, more sophisticated methods can generate more accurate matching.

In [23], the authors demonstrated that combinations of ALIKED with LG and GIM with LG yielded the best results on out-of-domain data. Other learning-based detectorless techniques, such as Dust3r [24] and Mast3r [25] process the entire pipeline at once, making them highly computationally intensive and impractical for large datasets on standard machines.

III. ROBOTIC PLATFORM FOR 3D GENERATION

This section outlines our robotic arm platform for multi-view image acquisition and 3D reconstruction in MIS, as

seen in Figure 2. We describe the design of the robotic arm, imaging and recording systems, introduce the various scanning trajectories implemented using the robot and discuss our hand-eye calibration method.

A. Robotic Arm

The platform utilises a Kinova Gen 3 7-Degrees of Freedom (DoF) robotic arm¹. The arm has a maximum reach of 902 mm and a maximum speed of 0.5 m/s at the end effector. Unlike many other robotic arms, the actuators can rotate infinitely, allowing more of the workspace to be covered by the Kinova making it ideal for our application of capturing the different organs from different angles.

We interface with the robot using a modified version of ros2-kortex package². The platform uses the robotic manipulation platform MoveIt2³ [26] for motion planning and kinematics control. A custom `moveit_config` was created to suit our robot-laparoscope configuration.

B. Imaging

Our imaging system uses a FLIR Blackfly S USB3 (BFS-U3-50S5C-C, Teledyne FLIR, Wilsonville, Oregon, USA) RGB camera custom mounted to a (HOPKINS®Telescope 26003 AGA, Karl Storz SE & Co. KG, Tuttlingen, Germany). This 5-megapixel camera has a resolution of 2448x2048 giving us optimal data for further 3D reconstructions. As seen in Figure 2, the laparoscope is mounted directly to the Kinova robotic arm using 3D-printed and laser-cut brackets. We consider two different light source settings for our study: the Storz laparoscopic light source (Storz D-LIGHT C 201336 20) attached directly to the laparoscope by fibre optic light cable (Storz 495 NCS) and the overhead ceiling-mounted surgical lights (Maquet Volista Surgical Light, Maquet GmbH, Rastatt, Germany). The overhead surgical light source evenly illuminates the image and eliminates vignetting effects visible when using the laparoscopic light source only. Whilst the surgical overhead light source is not realistic for MIS, it gives an ideal set of lighting conditions to compare to.

C. Trajectories

The aim of the robot’s laparoscopic multi-view acquisition is to image the specimen organ from various angles, ensuring full surface coverage at least once. We represent this acquisition process as a sphere with the sample positioned at the centre. In Figure 2.b, we depict this using two spherical scanning trajectories: Open-Close and Open-Far. The key difference between them is the variation in the distance to the specimen, where the Open-close distance ($d_{lap}^{open-close}$) is shorter than the Open-Far distance ($d_{lap}^{open-far}$). While this setup provides excellent coverage, it is only suitable for open surgery where there are no constraints on the surgical field.

To achieve these spherical trajectories we set a remote centre of motion (RCM) colinear, but external to the laparoscope

and place it at the centre of these virtual spheres. Thus the tip of the laparoscope moves in a spherical trajectory around the RCM and all poses can be simply defined as an orientation of the RCM.

In laparoscopic surgery, however, the endoscope’s access is limited by the trocar — a single entry point through the skin surface. Therefore we define a third trajectory, the Trocar trajectory, to replicate this scenario. Although this is more clinically realistic, it introduces significant challenges for organ imaging, due to reduced field of view (FoV).

Our platform relies on MoveIt2 which utilises the Open Motion Planning Library (OMPL) [27], [28] to plan these constrained trajectories, specifically using the RRTConnect planner. We use the default inverse kinematic (IK) solver in MoveIt2 which is the Orocos Kinematics and Dynamics plugin [29]. Given the non-uniqueness of RCM pose solutions with a 7-DoF, we change the kinematics solver joint states seed to the current position rather than all zeroes to prevent awkward IK solutions that require large movements from the current state.

D. Pose Generation Using Fibonacci Sphere Sampling

Achieving an even distribution of points on a spherical surface is essential for optimal coverage and accurate 3D reconstruction. Traditional methods, like uniformly sampling azimuthal and altitude angles, often result in uneven distributions, causing point clustering near the poles. This leads to sampling biases and inefficiencies, particularly in multi-view image acquisition for 3D reconstruction. We employed the Fibonacci sphere sampling method to generate evenly distributed poses on a spherical surface [30]. This approach provides a uniform distribution of points across a sphere, avoiding clustering near the poles as seen in Figure 2.b. The Fibonacci sphere is generated by calculating the azimuthal angle θ for each point on the sphere. This angle is incremented by the golden angle $\phi = \pi(3 - \sqrt{5})$, ensuring uniform spacing. The vertical position y is distributed evenly between 1 and -1.

To maintain focus on a region of interest and to allow adjustment for different OR settings, we limit the poses for all three trajectories to those within a specified angular range, defined by an angle limit θ_{max} . This ensures that only points with an elevation angle greater than $90^\circ - \theta_{max}$ are included, thereby restricting poses to the top of the sphere. Finally, the orientation of each pose is computed by aligning the axis colinear to the laparoscope with the vector pointing from the centre of the sphere to the sampled point.

E. Data Recording

We use our custom-developed Python app built on the FLIR Spinnaker Software Development Kit (SDK) to pre-view and capture data. The app can capture images and video frames. Each video frame is saved as a numpy file and frame information such as exposure time and current framerate is stored in a csv frame log. The RCM and end-effector positions of the robot are also saved for analysis.

¹www.kinovarobotics.com

²https://github.com/Kinovarobotics/ros2_kortex

³<https://moveit.ai>

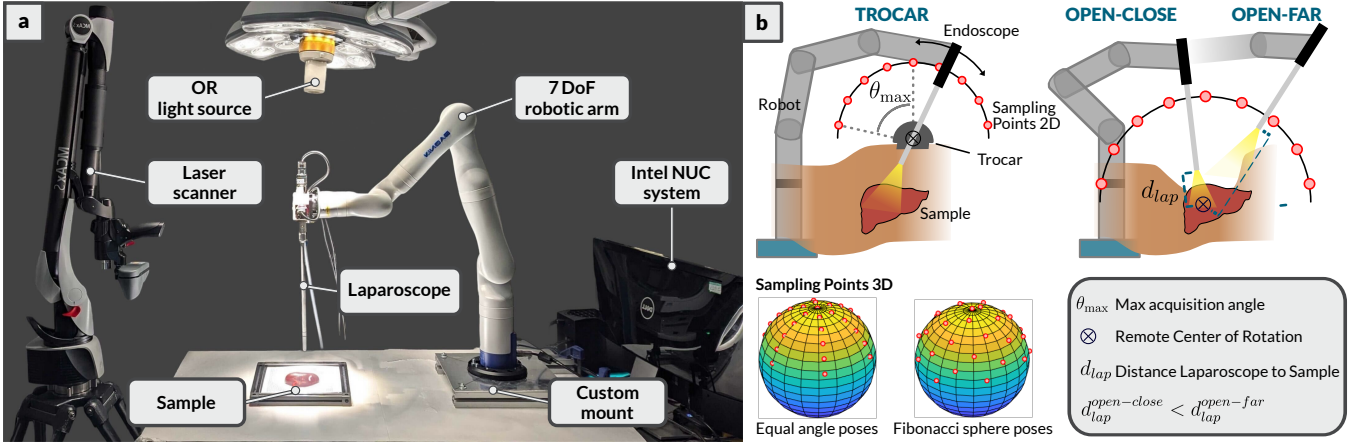


Fig. 2. **a)** Annotated figure showing the robotic platform. The robot is attached to the table using a custom mount. The laparoscope optical system is attached to the robot with 3D printed and laser-cut parts. All trajectory control and data capture are handled by an Intel NUC. **b)** Depiction of acquisition setup and the three trajectories: Trocar, Open-Close and Open-Far. Additionally, the sampling points in 3D are depicted for both equal angle poses where poses are calculated by sequentially incrementing the azimuth and altitude angles by fixed amounts and Fibonacci sphere poses which are more even coverage over the imaging sphere.

F. Hand-Eye Calibration

An additional dataset was captured on a ChAruco board using all three trajectories to ensure a good calibration. Each frame of this dataset underwent min-max normalisation to enhance the ChAruco board detection. The intrinsic calibration of the camera was obtained using OpenCV, with a reprojection error of 0.88 pixels. The robot was then hand-eye calibrated using a dual quaternion method [31] to obtain the transform from the end-effector of the robotic arm to the principal point of the camera.

IV. DATA ACQUISITION

For this work, we used a total of eight *ex-vivo* ovine organs: six kidneys and two livers. RGB frames from each organ set can be seen in Figure 3.a. Four of the kidneys were paired to give a total of six organ sets. Each organ was placed on a tray with a featured background to aid the SfM pipeline. Three different trajectories were used to image each organ set as visualised in Figure 2:

- 1) Trocar: the RCM was placed ~ 120 mm above the centre of the sample. This leaves the tip ~ 80 mm above the sample creating a realistic MIS scenario
- 2) Open-Close: the RCM is placed in the sample with $d_{lap} = 80$ mm
- 3) Open-Far: the RCM is placed in the sample with $d_{lap} = 120$ mm for a wider FoV.

The organs were imaged with two different light source configurations: laparoscopic light source only (Laparos.) and a combination of Laparos. and the overhead surgical light source (Surgical) seen in Figure 2. For the kidney datasets, each of the trajectories was performed with both light source configurations leading to six videos per organ set and twenty-four total videos. For the liver sample sets only the Trocar and Open-Far trajectory were performed, because the livers were larger the Open-Close trajectory was skipped to minimise the risk of collisions. This led to four

videos per liver, eight in total and an overall dataset size of 32 videos.

In tackling issues with ground truth, as detailed in our related work, we implement a laser scanner to acquire highly accurate 3D meshes and point clouds from our samples. We use the Nikon H120 ModelMaker and MCAX S (Nikon Corporation, Tokyo, Japan) for this approach. The laser scanning system has an accuracy of down to $7\mu\text{m}$ ⁴ giving us the ability for to precisely evaluate our methods. This accuracy is greater than both structured light and the CT ground truths supplied by current datasets as structured light/stereo depth estimation is limited by the resolution of the cameras and feature matching algorithms and CT scanners have larger voxel sizes and requires a segmentation step for a 3D model for comparison that could introduce errors. A full 3D reconstruction ground truth does allow evaluation of a whole pipeline in comparison to solely depth maps, as projection from depth maps can introduce errors. Depth maps can be extracted from a ground truth point cloud provided camera poses and intrinsics, which does however rely on good registration from laser scanner to point cloud.

V. 3D RECONSTRUCTION

This section details our pipeline for producing 3D reconstructions from our robotic arm pipeline as seen in Figure 3. To perform the 3D reconstruction, we utilised two image feature extraction and matching methods, GIM-LG and ALIKED-LG. GIM-LG uses a handcrafted feature extractor and a retrained matching component, LG, following the GIM training framework. ALIKED is a lightweight CNN-based keypoint detector and descriptor extractor that we paired with the LG matching component. These models were chosen due to their performance in [23], particularly in out-of-domain challenges. For comparison, we also paired LG

⁴<https://industry.nikon.com/en-us/products/3d-laser-scanners/manual-3d-scanning/modelmaker-h120/>

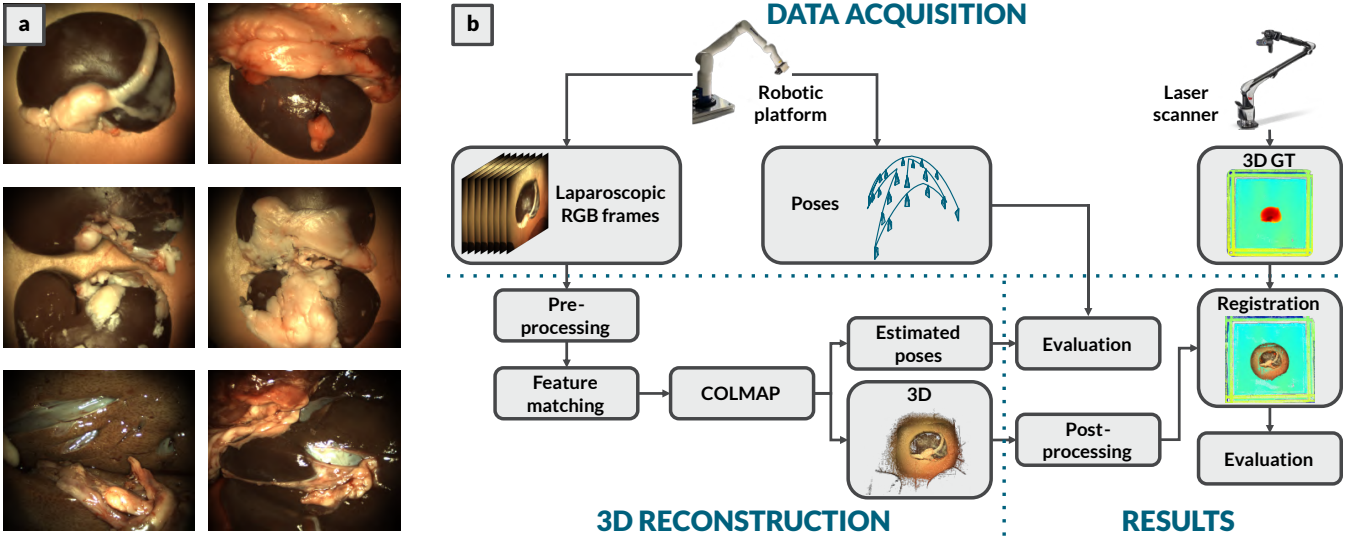


Fig. 3. **a)** An RGB frame from each of the 6 organ sample sets. Row 1&2 show different kidney samples. In row 3 we show a section of two liver samples. **b)** Data acquisition: A summary of all the data collected by our platform. 3D Reconstruction: Our 3D reconstruction pipeline for processing our data. Results: Evaluation of the 3D reconstructions by comparing to acquired ground truth data.

with SIFT [22], a commonly used feature detector. All the data was processed on a workstation with an AMD Ryzen Threadripper PRO 5975WX CPU and two NVIDIA RTX A6000 GPUs. Following this step we convert the data to standard COLMAP data structure and create sparse and dense reconstructions.

1) *Structure from Motion:* The images are undistorted using calibration data, and each video, with an average of 909 frames, is sub-sampled to 100 frames to reduce computational complexity due to high frame correlation. To generate a list of image pairs, we use the method from [23] by pairing sequential frames using a sliding window. We enhance the matching process by utilising a pre-trained DINOv2-SALAD [32] model to generate extra pairs. DINOv2-SALAD acts on each frame in the sub-sampled dataset and finds correspondences to other frames in the set. DINOv2 is employed for local feature extraction, while SALAD aggregates these local features to clusters and uses the optimal transport method to generate global features. Following this approach resulted in an average of 1169 pairs per dataset. Subsequent image pairs were fed to the image matchers ALIKED-LG, GIM-LG and SIFT-LG which returned matches for each pair. We then utilise the incremental SfM from COLMAP to create dense 3D reconstructions and estimated camera poses which can be evaluated in comparison to the ground truth. The hand-eye calibrated poses were not used in the pipeline as we use them for evaluation of the predicted poses.

2) *Post-processing:* Prior to comparison, the dense point clouds undergo a post-processing step. Due to our pipeline returning relative point clouds, the point clouds are manually registered to the laser scan ground truth using Open3D [33] by manually selecting matching points in both point clouds before undergoing iterative closest point (ICP) registration with the laser scan to refine the registration. Manually

registered point clouds are downsampled to 0.5 mm and cleaned from statistical outliers using Open3D. The mean distance to its k nearest neighbours is calculated using a KD-Tree for efficient neighbour queries for every point. Subsequently, the global mean and standard deviation are computed for all points. Points are considered outliers if their mean neighbour displacements exceed a threshold defined as the population mean plus a multiple of the standard deviation. This method removes isolated noise while preserving the point cloud structure, making it suitable for denoising in 3D reconstruction workflows. For this, we set $k = 20$ and $std_ratio = 1.0$ to maintain data quality. Finally, points more than 60 mm from the centroid are removed. Finally, we use Open3D's Point-to-Plane ICP registration [34] to register our reconstruction with the ground truth with the default Tukey Loss with $k = 1$. This uses the normals of the target scan, obtained directly from the laser scanner, in its objective function to increase the fidelity of the ICP algorithm.

While the majority of the reconstructions were successful, 12 out of 96 were excluded due to issues in reconstruction with the SIFT-LG method account for 50% of failures. Half of all exclusions were due to insufficient point cloud data resulting from too few features detected, and the remaining due to excessive noise, particularly in the trocar trajectory, which posed challenges for feature detection and surface reconstruction due to restricted views.

VI. RESULTS

A. Qualitative Results

In this section, we present our qualitative results and findings. In Figure 4 two representative cases are shown for a liver and a kidney. The first case involves a kidney acquired using the Open-Far trajectory with overhead OR lighting, processed using the ALIKED-LG matcher. The second case involves a liver acquired using the trocar trajectory with

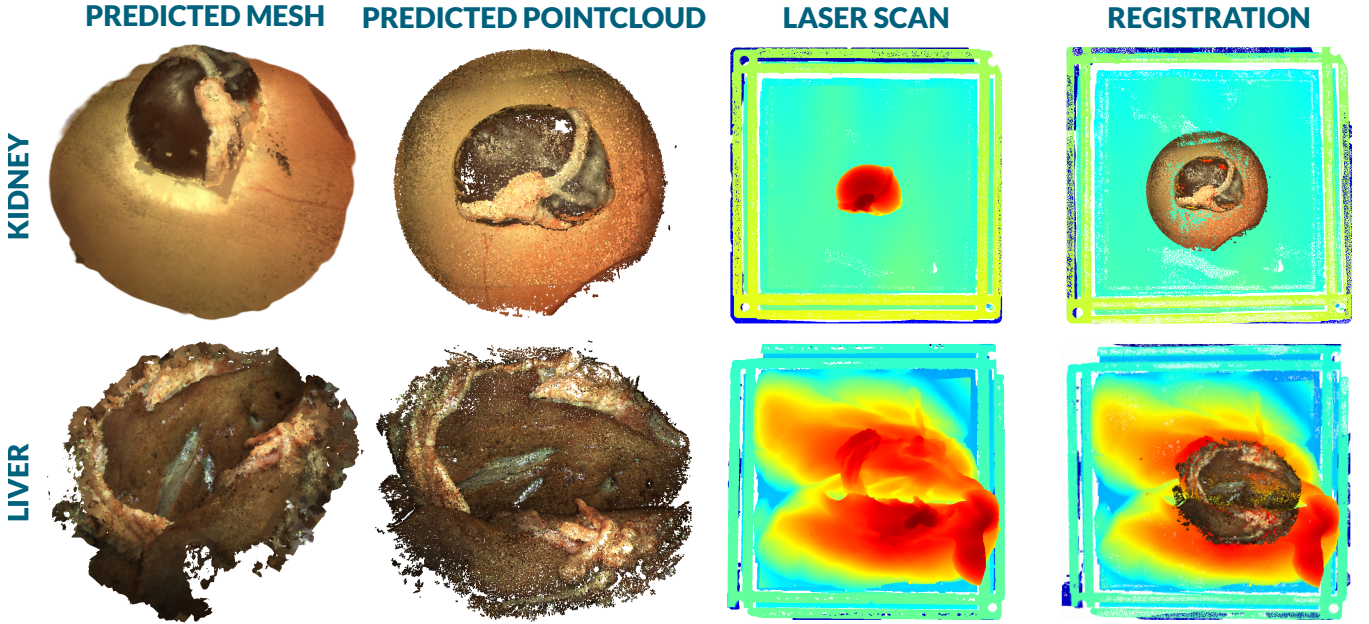


Fig. 4. 3D reconstructions of a kidney and liver obtained using different trajectories and lighting conditions. For the kidney (row 1), data was captured using the Open-Far trajectory under operating room lighting, and processed with the ALIKED-LG image matcher. The liver (row 2) was captured using the trocar trajectory under laparoscopic lighting and processed using the GIM-LG matcher. In both cases, the predicted 3D models (col 1&2) are compared to the ground truth laser scans (col 3) and the post-processed, aligned reconstructions (col 4).

laparoscopic lighting, processed using the GIM-LG matcher. Both methods resulted in visually accurate 3D reconstructions despite the differences in acquisition trajectories and lighting conditions. While the overall reconstructions appear good, we noticed small holes in some areas of the point clouds. These gaps are minor and do not significantly affect how the 3D models can be used, but they may slightly reduce the visual quality. For improved visualisation, we used Poisson meshes, which helped fill in some of the gaps and gave us cleaner-looking models. By observing the location of these holes it appears that one of the main challenges in the 3D pipeline is dealing with the dark, smooth surfaces of the organ and specular highlights. These surfaces, especially under laparoscopic lighting, made it harder for the algorithms to detect enough matching features, particularly when we used the limited perspectives of the trocar trajectory. With fewer camera angles, there were more instances of occlusions and missing data compared to the wider Open-Close and Open-Far trajectories, where the broader FoV provided a clearer picture. Despite these difficulties with unreconstructed surfaces, the registrations between our predicted models and the ground truth laser scans appear to be visually well aligned with only minor discrepancies.

B. 3D Reconstruction Results

1) *Metrics:* In evaluating the performance of point cloud registration to a ground truth laser scan, we employed three widely used distance metrics in millimetres: Chamfer distance, Hausdorff distance, and Root Mean Squared Error (RMSE). Each metric provides a different aspect of the registration quality: Chamfer distance measures average minimum distances between points, Hausdorff distance captures

maximum deviations, and RMSE reflects average point-wise errors. Together, they give us a comprehensive view of how closely our reconstructions match the ground truth.

Due to gaps and holes in the incomplete laser scan, we excluded the top 5% of distances from the metric calculations. This step prevents artificially inflated errors from points in the source cloud that are not covered by the target cloud. Tables II and III presents the quantitative evaluation of our point cloud registrations against the ground truth laser scans. Table II compares the performance of different methods — SIFT-LG, GIM-LG, and ALIKED-LG — across the two lighting conditions (operating room and laparoscopic lighting) for both kidney and liver datasets averaged across all trajectories.

2) *Differences in Organ Reconstructions:* In table II we show the results of the organ 3D reconstruction for the different methods and datasets. Overall the reconstruction results for the different organs and methods show consistent finding with ALIKED-LG and GIM-LG outperforming the SIFT-LG baseline method consistently. Only for the Kidney dataset under the surgical light setting the SIFT-LG shows better Chamfer results (-0.112) and RMSE (-0.166) compared to the ALIKED-LG method. The sharper transitions and irregularities at the kidney edges make accurate feature matching often more difficult and ALIKED-LG seems to struggle in these scenarios. On the Liver dataset we see that the ALIKED-LG model outperforms GIM-LG and SIFT-LG by a large margin.

3) *Lighting Conditions:* Table II highlights the influence of lighting conditions on registration metrics. Surgical lighting, offering broader and more even illumination, generally produced better results, particularly with lower Chamfer,

TABLE II

AVERAGE METRICS USING THE LAPAROS. AND SURGICAL LIGHT SOURCE. BEST RESULTS HIGHLIGHTED IN BOLD AND BEST FOR EACH LIGHT SOURCE SETTING INDIVIDUALLY IS UNDERScoreD.

Metric	Method	Surgical	Laparos.
Kidneys			
Chamfer	SIFT-LG	0.760	0.983
	GIM-LG	0.605	0.786
	ALIKED-LG	0.872	0.869
Hausdorff	SIFT-LG	2.626	3.783
	GIM-LG	2.017	2.922
	ALIKED-LG	3.090	3.261
RMSE	SIFT-LG	0.995	1.294
	GIM-LG	0.764	1.029
	ALIKED-LG	1.161	1.146
Livers			
Chamfer	SIFT-LG	1.571	1.735
	GIM-LG	0.686	1.225
	ALIKED-LG	0.551	0.588
Hausdorff	SIFT-LG	5.430	6.072
	GIM-LG	2.499	4.347
	ALIKED-LG	2.030	2.244
RMSE	SIFT-LG	2.068	2.284
	GIM-LG	0.892	1.588
	ALIKED-LG	0.720	0.769

TABLE III

AVERAGE METRICS ACROSS TRAJECTORIES FOR KIDNEYS AND LIVERS. THE BEST-PERFORMING METRICS FOR EACH ORGAN ACROSS ALL METHODS AND TRAJECTORIES ARE HIGHLIGHTED IN BOLD.

Metric	Method	Trocar	Open-close	Open-far
Kidneys				
Chamfer	SIFT-LG	0.974	0.787	0.855
	GIM-LG	0.844	0.669	0.581
	ALIKED-LG	0.815	0.801	0.981
Hausdorff	SIFT-LG	3.363	3.158	3.093
	GIM-LG	2.814	2.651	1.930
	ALIKED-LG	2.972	3.051	3.452
RMSE	SIFT-LG	1.246	1.041	1.147
	GIM-LG	1.078	0.882	0.735
	ALIKED-LG	1.059	1.058	1.320
Livers				
Chamfer	SIFT-LG	1.990	-	0.550
	GIM-LG	0.757	-	1.172
	ALIKED-LG	0.692	-	0.483
Hausdorff	SIFT-LG	6.902	-	2.112
	GIM-LG	2.721	-	4.181
	ALIKED-LG	2.391	-	1.973
RMSE	SIFT-LG	2.621	-	0.720
	GIM-LG	0.969	-	1.530
	ALIKED-LG	0.876	-	0.653

Hausdorff, and RMSE values. In contrast, laparoscopic lighting, which is more focused and directional, led to slightly higher errors, especially in the Hausdorff distance, likely due to the introduction of shadows, uneven illumination, and pronounced vignetting. Despite these differences, both GIM-LG and ALIKED-LG exhibited strong performance across lighting conditions, with GIM-LG performing slightly better overall, particularly in the Chamfer (2.017 and 2.922) and RMSE (0.764 and 1.029) metrics on the kidney dataset. These results confirm that both methods are effective for 3D reconstruction in surgical environments, with GIM-LG showing especially consistent performance, without outliers, even in challenging lighting conditions.

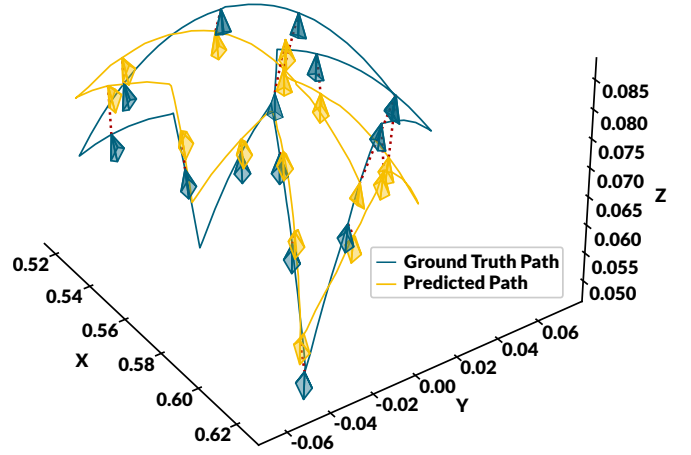


Fig. 5. A graph depicting a sub-sampled set of poses of the ground truth (blue) and predicted (yellow) poses for a kidney dataset with the OR light source and the open-far trajectory using the ALIKED-LG image matcher.

4) *Trajectories*: Table III presents the average metrics for each trajectory. Due to the larger size of the livers, no open-close trajectory was recorded to avoid collisions with the organ. The metric differences between the Open-close and Open-far datasets highlight that the choice of d_{lap} significantly impacts reconstruction quality, emphasizing the need for careful parameter selection. Among the trajectories, the trocar trajectory—being the most realistic—performed the worst, likely due to the limited number of views. However, when SIFT data was excluded, the average Chamfer distances across all organs were 0.797, 0.735, and 0.795 for the trocar, open-close, and open-far trajectories, respectively. This demonstrates that modern feature matching techniques can achieve comparable results even with realistic, patient-specific trajectories.

C. Pose Evaluation

We employed the Umeyama algorithm [35] to align our predicted poses with the ground truth for comparison. Figure 4 illustrates a subsampled set of pose estimations from a kidney dataset using an open-close trajectory, with the ALIKED-LG feature matching version of the pipeline. Overall, the poses were accurate, with translation estimations appearing slightly better than rotations. The relative pose error (RPE) for rotation was 0.0161 radians using ALIKED-LG, 0.0032 for GIM-LG, and 0.0290. For translations, the RPE was 0.265 mm for ALIKED-LG, 0.285 mm, and 0.245 mm for GIM-LG.

On average, 88.78% of frames were predicted, with a standard deviation of 27.85%, which can be attributed to a few anomalous cases with fewer than 15 frames having predicted poses. Across all datasets, 81.25% successfully predicted poses for all frames, with GIM-LG slightly outperforming ALIKED-LG at 90.95% compared to 86.60%. This highlights the robustness of both methods, especially GIM-LG, in feature matching and pose prediction.

VII. CONCLUSIONS

In this work, we have customized a robotic arm platform for medical applications, demonstrated a versatile acquisition protocol, and utilized multi-view images for 3D reconstructions. Our platform has proven effective for efficiently and reliably collecting extensive datasets, streamlining the data acquisition process while ensuring high realism and adaptability through relevant metrics. This platform holds significant potential for advancing research, particularly in challenging environments involving smoke, blood, tool occlusions, and deformable tissue. Future developments may focus on adapting the platform to these complex surgical scenarios, with an emphasis on real-time processing and further enhancement of data quality.

REFERENCES

- [1] L. Maier-Hein, S. S. Vedula, S. Speidel, N. Navab, *et al.*, “Surgical data science for next-generation interventions,” *Nature Biomedical Engineering*, vol. 1, pp. 691–696, 2017. [Online]. Available: <https://doi.org/10.1038/s41551-017-0132-7>
- [2] S. Nicolau, L. Soler, D. Mutter, and J. Marescaux, “Augmented reality in laparoscopic surgical oncology,” *Surgical Oncology*, vol. 20, no. 3, pp. 189–201, 2011, special Issue: Education for Cancer Surgeons. [Online]. Available: <https://www.sciencedirect.com/science/article/pii/S0960740411000521>
- [3] N. Chong, Y. Si, W. Zhao, Q. Zhang, *et al.*, “Virtual reality application for laparoscope in clinical surgery based on siamese network and census transformation,” in *MICAD*, ser. Lecture Notes in Electrical Engineering, R. Su, Y.-D. Zhang, and H. Liu, Eds., vol. 784. Springer, 2021, pp. 59–70. [Online]. Available: <http://dblp.uni-trier.de/db/conf/micad2/micad2021.html#ChongSZZYZ21>
- [4] S. Overley, S. Cho, A. Mehta, and P. Arnold, “Navigation and robotics in spinal surgery: Where are we now?” *Neurosurgery*, vol. 80, pp. S86–S99, 03 2017.
- [5] L. Bianchi, U. Barbaresi, L. Cencenelli, B. Bortolani, *et al.*, “The impact of 3d digital reconstruction on the surgical planning of partial nephrectomy: A case-control study. still time for a novel surgical trend?” 2020.
- [6] T. L. Bobrow, M. Golhar, R. Vijayan, V. S. Akshintala, *et al.*, “Colonoscopy 3d video dataset with paired depth from 2d-3d registration,” *Medical Image Analysis*, p. 102956, 2023.
- [7] M. Allan, J. Mcleod, C. Wang, J. C. Rosenthal, *et al.*, “Stereo correspondence and reconstruction of endoscopic data challenge,” *arXiv preprint arXiv:2101.01133*, 2021.
- [8] P. E. Edwards, D. Psychogios, S. Speidel, L. Maier-Hein, *et al.*, “Serv-ct: A disparity dataset from cone-beam ct for validation of endoscopic 3d reconstruction,” *Medical image analysis*, vol. 76, p. 102302, 2022.
- [9] M. Hayoz, C. Hahne, M. Gallardo, D. Candinas, *et al.*, “Learning how to robustly estimate camera pose in endoscopic videos,” *International journal of computer assisted radiology and surgery*, vol. 18, no. 7, pp. 1185–1192, 2023.
- [10] X. Zhao, X. Wu, W. Chen, P. C. Y. Chen, *et al.*, “Aliked: A lighter keypoint and descriptor extraction network via deformable transformation,” *IEEE Transactions on Instrumentation and Measurement*, vol. 72, pp. 1–16, 2023.
- [11] X. Shen, Z. Cai, W. Yin, M. Müller, *et al.*, “Gim: Learning generalizable image matcher from internet videos,” *arXiv preprint arXiv:2402.11095*, 2024.
- [12] P. Lindenberger, P.-E. Sarlin, and M. Pollefeys, “Lightglue: Local feature matching at light speed,” in *2023 IEEE/CVF International Conference on Computer Vision (ICCV)*, 2023, pp. 17 581–17 592.
- [13] J. L. Schönberger and J.-M. Frahm, “Structure-from-motion revisited,” in *Conference on Computer Vision and Pattern Recognition (CVPR)*, 2016.
- [14] J. L. Schönberger, E. Zheng, M. Pollefeys, and J.-M. Frahm, “Pixel-wise view selection for unstructured multi-view stereo,” in *European Conference on Computer Vision (ECCV)*, 2016.
- [15] R. D. Howe and Y. Matsuoka, “Robotics for surgery,” *Annual review of biomedical engineering*, vol. 1, no. 1, pp. 211–240, 1999.
- [16] V. Vitiello, S.-L. Lee, T. P. Cundy, and G.-Z. Yang, “Emerging robotic platforms for minimally invasive surgery,” *IEEE reviews in biomedical engineering*, vol. 6, pp. 111–126, 2012.
- [17] A. Attanasio, B. Scaglioni, E. De Momi, P. Fiorini, *et al.*, “Autonomy in surgical robotics,” *Annual Review of Control, Robotics, and Autonomous Systems*, vol. 4, no. 1, pp. 651–679, 2021.
- [18] O. Wagner, M. Hagen, A. Kurmann, S. Horgan, *et al.*, “Three-dimensional vision enhances task performance independently of the surgical method,” *Surgical endoscopy*, vol. 26, pp. 2961–2968, 2012.
- [19] T. Haidegger, S. Speidel, D. Stoyanov, and R. M. Satava, “Robot-assisted minimally invasive surgery—surgical robotics in the data age,” *Proceedings of the IEEE*, vol. 110, no. 7, pp. 835–846, 2022.
- [20] L. Maier-Hein, A. Groch, A. Bartoli, S. Bodenstedt, *et al.*, “Comparative validation of single-shot optical techniques for laparoscopic 3-d surface reconstruction,” *IEEE transactions on medical imaging*, vol. 33, no. 10, pp. 1913–1930, 2014.
- [21] M. Xu, Z. Guo, A. Wang, L. Bai, *et al.*, “A review of 3d reconstruction techniques for deformable tissues in robotic surgery,” *arXiv preprint arXiv:2408.04426*, 2024.
- [22] G. Lowe, “Sift-the scale invariant feature transform,” *Int. J.*, vol. 2, no. 91-110, p. 2, 2004.
- [23] S. Bonilla, C. Di Vece, R. Daher, X. Ju, *et al.*, “Mismatched: Evaluating the limits of image matching approaches and benchmarks,” *arXiv preprint arXiv:2408.16445*, 2024.
- [24] S. Wang, V. Leroy, Y. Cabon, B. Chidlovskii, *et al.*, “Dust3r: Geometric 3d vision made easy,” in *CVPR*, 2024.
- [25] V. Leroy, Y. Cabon, and J. Revaud, “Grounding image matching in 3d with mast3r,” 2024.
- [26] D. Coleman, I. Sucan, S. Chitta, and N. Correll, “Reducing the barrier to entry of complex robotic software: a moveit! case study,” *arXiv preprint arXiv:1404.3785*, 2014.
- [27] I. A. Sucan, M. Moll, and L. E. Kavraki, “The open motion planning library,” *IEEE Robotics & Automation Magazine*, vol. 19, no. 4, pp. 72–82, 2012.
- [28] Z. Kingston, M. Moll, and L. E. Kavraki, “Exploring implicit spaces for constrained sampling-based planning,” *The International Journal of Robotics Research*, vol. 38, no. 10-11, pp. 1151–1178, 2019.
- [29] R. Smits, “KDL: Kinematics and Dynamics Library,” <http://www.orocos.org/kdl>.
- [30] B. Keinert, M. Innmann, M. Sängner, and M. Stamminger, “Spherical fibonacci mapping,” *ACM Transactions on Graphics (TOG)*, vol. 34, no. 6, pp. 1–7, 2015.
- [31] K. Daniilidis, “Hand-eye calibration using dual quaternions,” *The International Journal of Robotics Research*, vol. 18, no. 3, pp. 286–298, 1999.
- [32] S. Izquierdo and J. Civera, “Optimal transport aggregation for visual place recognition,” in *Proceedings of the IEEE/CVF Conference on Computer Vision and Pattern Recognition*, 2024, pp. 17 658–17 668.
- [33] Q.-Y. Zhou, J. Park, and V. Koltun, “Open3D: A modern library for 3D data processing,” *arXiv:1801.09847*, 2018.
- [34] Y. Chen and G. Medioni, “Object modelling by registration of multiple range images,” *Image and vision computing*, vol. 10, no. 3, pp. 145–155, 1992.
- [35] S. Umeyama, “Least-squares estimation of transformation parameters between two point patterns,” *IEEE Transactions on Pattern Analysis & Machine Intelligence*, vol. 13, no. 04, pp. 376–380, 1991.